Atmos. Chem. Phys., 25, 13019–13035, 2025 https://doi.org/10.5194/acp-25-13019-2025 © Author(s) 2025. This work is distributed under the Creative Commons Attribution 4.0 License.





Surface—bulk photochemical coupling of nonanoic acid and 4-benzoylbenzoic acid: the dual role of the photosensitizer and environmental influences

Ahmed Abdelmonem¹, Dana Glikman², Yiwei Gong¹, Björn Braunschweig², Harald Saathoff¹, Johannes Lützenkirchen³, and Mohammed H. Fawey⁴

¹Institute of Meteorology and Climate Research, Karlsruhe Institute of Technology (KIT),
76344 Eggenstein-Leopoldshafen, Germany

²Institute of Physical Chemistry and Center for Soft Nanoscience,
University of Münster, 48149 Münster, Germany

³Institute of Nuclear Wastes Disposal, Karlsruhe Institute of Technology (KIT),
76344 Eggenstein-Leopoldshafen, Germany

⁴Physics Department, Faculty of Science, Sohag University, 82524 Sohag, Egypt

Correspondence: Ahmed Abdelmonem (ahmed.abdelmonem@kit.edu)

Received: 15 March 2025 – Discussion started: 26 March 2025 Revised: 15 August 2025 – Accepted: 15 August 2025 – Published: 20 October 2025

Abstract. Organic compounds concentrated at air—water interfaces, such as the sea-surface microlayer (SML), or aerosol and cloud droplets, are key contributors to complex photochemical reactions. Nonanoic acid (NA) is surface active, and 4-benzoylbenzoic acid (4-BBA) is a photosensitizer. This study combines investigations at the air-water interface by sum-frequency generation (SFG) spectroscopy and in the liquid and gas phases by mass spectrometry (MS) to study the photochemical interactions of both substances at the air-water interface. We identify a novel interfacial aromatic signal via SFG, revealing surface-localized photoproducts previously undetected (C₉H₁₀O₅). The study demonstrates that 4-BBA not only acts as photosensitizer but also undergoes photodegradation. Our experiments show the critical influence of the UV portion of the solar spectrum on photoproduct formation, as significant amounts of benzene (C_6H_6) and benzaldehyde (C_7H_6O) were detected as degradation products of 4-BBA in the gas phase particularly for the lowest wavelengths (280-310 nm). In the liquid phase, we identified the following photoreaction products: $C_8H_{12}O_4$, $C_8H_{12}O_5$, $C_9H_{10}O_5$, $C_9H_{14}O_3$, $C_9H_{16}O_3$, $C_9H_{16}O_4$, and $C_{10}H_{14}O_4$. Among these, $C_8H_{12}O_4$, $C_9H_{10}O_5$, and $C_9H_{16}O_3$ were most enhanced (by a factor of ~ 11) in the presence of 4-BBA, with $C_9H_{10}O_5$ strongly dependent on the presence of oxygen. The formation of C₉H₁₀O₅ increased at shorter wavelengths due to photodegradation of 4-BBA, while C₈H₁₂O₄ and C₉H₁₆O₃ were dominant at longer wavelengths, consistent with photooxidation of NA. While pH and salinity were not varied systematically in this study, we found that decreasing the pH from 8 to 5.4 affected the water restructuring at the interface and increased the rate of photoproduct formation. Increasing salinity from zero to \sim 38 ppt enhanced the photoreaction rates by a factor of 2. These findings highlight the importance of environmental factors in modeling interfacial photochemistry and demonstrate how SFG reveals surface-bulk coupling relevant to product formation in diverse aquatic systems.

1 Introduction

The Earth's climate system is impacted by atmospheric chemistry and air-water interactions, which affect the energy budget through scattering of sunlight and absorption of thermal radiation (Meerkötter and Vázquez-Navarro, 2012). Atmospheric aerosols have both natural and anthropogenic sources which vary depending on the location, time of year, and meteorological conditions (Boucher, 2015). These sources include dust, sea spray, volcanic ash, wildfires, biological particles, industrial and agricultural processes, transportation, and waste disposal (Ouafo-Leumbe et al., 2018). It has been estimated that the secondary reaction products of volatile organic compounds (VOCs) can contribute significantly to secondary atmospheric aerosols (SOAs), influencing cloud properties and radiative balance, with the vast majority originating from biogenic sources (Wang et al., 2023). Moreover, up to 91.9 Tg Cyr⁻¹ of organic vapors could be emitted from the oceans into the marine atmosphere and have a potential contribution to organic aerosol mass of more than 60 % over the remote ocean (Brüggemann et al., 2018).

Organic compounds are highly concentrated at the seasurface microlayer (SML) or as surfactant coatings on cloud droplets (Carpenter and Nightingale, 2015). The SML contains dissolved organic carbon (DOC) and chromophoric and fluorescent dissolved organic matter (CDOM and FDOM, respectively), which are transferred to the atmosphere via sea spray aerosol (SSA) (Yang et al., 2022). While sea salt dominates the cloud condensation nuclei (CCN) activity of SSA, organic matter contributes primarily to aerosol mass (Hendrickson et al., 2021). Biological and physicochemical processes in the SML, such as the enrichment of longand medium-chain fatty acids (LCFAs and MCFAs), further enhance SSA surface activity and influence atmospheric processes (Dommer et al., 2024). Atmospheric nutrient deposition can also influence short-term enrichments of organic matter in the SML, particularly when associated with biomass burning emissions (Milinković et al., 2022).

The air-water interface is ubiquitous in the environment and frequently exposed to the atmosphere and/or solar light, making photochemical interactions highly probable (Liss and Duce, 2005), particularly in the presence of lightabsorbing CDOM at surfaces. It was previously believed that CDOM is more concentrated at surfaces than in the bulk (Carlson, 1983; Carlson and Mayer, 1980); however, more recent studies have shown that CDOM is not always enriched at the surface (van Pinxteren et al., 2020; Stolle et al., 2020; Tilstone et al., 2010). Organic coatings on water surfaces can increase the concentration of natural photosensitizers and facilitate the generation of reactive species and VOCs through photochemical and oxidative processes (Tinel et al., 2016; Wang et al., 2023). Ozone oxidation in the SML, for example, generates VOCs such as acetone and aldehydes (Wang et al., 2023). Photobleaching of CDOM leads to the formation of low-molecular-weight DOM and CO₂, with reaction rates dependent on solar radiation intensity and DOM composition (Yang et al., 2022). This process is influenced by the intensity and duration of solar radiation, as well as the composition of DOM, which varies seasonally and spatially.

Solar radiation and wind intensity shape SML chemistry by modifying organic content and regulating air-sea CO2 exchange (Stolle et al., 2020). Natural bodies of water exhibit a range of pH and salinity values typically between pH 6 and 9 (Dickson, 1993; Jiang et al., 2019) and salinity between 0.5 ppt (parts per thousand) and 35 ppt (Dommer et al., 2024; Millero et al., 2008), although hydrogeochemical factors can cause deviations (Cui et al., 2022). The presence of mineral ions such as calcium, magnesium, sodium, chloride, and sulfate further influences the salinity and pH, thereby modulating the surface activity of the organic compounds (Covington and Whitfield, 1988; Marion et al., 2011). These geochemical parameters play vital roles in processes such as rock weathering, mineral precipitation, gas solubility, corrosion, biological shell formation, and water hardness (Morgan, 1995). Prior reports on the existence and significance of organic layers at air-water interfaces, such as the SML (Bernard et al., 2016; Ciuraru et al., 2015; Mmereki and Donaldson, 2002; Tinel et al., 2016) and sea spray (Sellegri et al., 2006; Wilson et al., 2015), emphasized the need to investigate this critical interface, particularly at the molecular level and under atmospheric conditions. Recent studies have highlighted the critical role of ocean biogeochemistry in shaping atmospheric composition and influencing aerosol-cloud interactions. In particular, the sea-surface microlayer has been recognized as a key interface for biologically driven gas emissions, with important implications for their representation in large-scale atmospheric models (Tinel et al., 2023). Moreover, oceanic biogeochemical processes have been shown to affect aerosol formation and cloud properties, thereby contributing to climate-relevant feedback mechanisms (Sellegri et al., 2024). Despite numerous studies aimed at investigating the emission and uptake of gases and aerosols in the atmosphere, limited information is available on the molecular composition and structure of surface entities (e.g., adsorbed on cloud droplets or sea surfaces) and their role in influencing interactions. A deeper understanding is still needed, as interfacial chemistry strongly governs atmospheric reactivity.

The air—water surface interactions occur in a variety of bodies of water and involve both biogenic and abiotic emissions (Bernard et al., 2016; Brüggemann et al., 2018), with organic materials from the SML being emitted into the atmosphere through bubble bursting and forming sea spray aerosols (Gantt and Meskhidze, 2013; Sellegri et al., 2006). These organic materials can be oxidized in the air and contribute to the creation of SOAs, which can then act as ice nuclei in mixed-phase clouds and high-altitude ice clouds (Liss and Duce, 2005). Tinel et al. (2016) demonstrated that the photosensitized degradation of fatty acids at the air—water interface, specifically nonanoic acid (NA) in the pres-

ence of 4-benzoylbenzoic acid (4-BBA) and imidazole-2-carboxaldehyde as model systems, enhances VOC emissions and secondary aerosol formation (Tinel et al., 2016). A subsequent study by Alpert et al. (2017) reported the formation of SOA particles through photochemical reactions and ozonolysis of saturated long-chain fatty acids and alcohol surfactants at the water surface (Alpert et al., 2017). More recently, Freeman-Gallant et al. (2024) showed that the efficiency of NA photooxidation in thin films depends on the type of organic photosensitizer, with 4-BBA identified as the most effective among those tested (Freeman-Gallant et al., 2024).

Previous studies primarily employed chemical, elemental and linear spectroscopic methods (such as UV–visible absorption, laser-induced fluorescence, and mass spectrometry). In contrast, molecular-level spectroscopic insights into interfacial chemistry under atmospheric conditions are scarce. In situ information on molecular alignment, bonding, and the formation or degradation of surface functional groups remains limited, yet it is critical for predicting the evolution of aerosols and water surfaces.

In this work, we combine sum-frequency generation (SFG) spectroscopy and mass spectrometry (MS) to probe the interfacial and bulk-phase photoproducts, respectively, of NA at the water surface in the presence of 4-BBA under varying irradiation spectra. We did not vary pH and salinity systematically but only report their impact for relatively small ranges. This system was particularly chosen due to the availability of prior bulk-phase study relying on linear techniques (Tinel et al., 2016), which verified that the interaction takes place at the water surface. Since SFG technique is suitable to probe the surface layer, we applied it here to probe the chemical and structural changes in the system. We employed an LED solar simulator with a spectrum closely resembling natural sunlight, improving upon earlier Xenon-lamp-based studies. The following section describes our experimental approach, followed by results and discussion beginning with the air-water interface and progressing to the molecular analysis of products in the aqueous and gas phases.

2 Experimental procedures

2.1 Materials

4-Benzoylbenzoic acid (4-BBA, 95 %,) and nonanoic acid (NA, 97 %) were purchased from Sigma Aldrich and Alfa Aesar, respectively. NA was used as received without further purification. We did not observe any evidence that impurities in NA influenced the photochemical reactions under the irradiation conditions used in this study. In contrast, 4-BBA was purified due to the presence of surface-active impurities. All solutions were prepared using ultrapure water (18.2 M Ω cm; total oxidizable carbon <5 ppb) that was obtained from a Milli-Q Reference A+ (Merck) purification system. Unless stated otherwise, all mixtures examined here are aqueous so-

lutions of 2 mM NA and 0.2 mM 4-BBA and with a total volume of 4 mL. The solution of 4-BBA was prepared using ultrasonication for 3 h and then steering over night at pH 7. The solution of NA was prepared using ultrasonication for 1 h. The pH was adjusted using 0.1 M NaOH from Fisher Chemical and controlled with SevenExcellence pH/Cond meter S470 from METTLER TOLEDO. Lab experiments were conducted under either synthetic air (ALPHA-GASTM, 20.5 \pm 0.5 % O_2 in N_2) or nitrogen gas (99.9999 %) from Air Liquid. The exact conditions for each experiment can be found in the Supplement.

2.2 Light source

To study photochemistry under atmospheric conditions, an irradiation source that closely mimics solar light is essential. It should be tunable to simulate different latitudes, altitudes, and seasonal variations, requiring a wavelength range starting at ~ 275 nm, adjustable intensity, and homogeneous illumination. For this purpose, a compact custombuilt LED-based solar simulator, the "Atmospheric Surface-Science Solar Simulator", was developed. The device is optimized to irradiate a 30 mm diameter sample area from a 50 mm distance, ensuring controlled photochemical reactions. The spectral characteristics of the simulator, including its spectral overlap with solar radiation and intensity adjustments, were determined using a calibrated spectrophotometer and a custom-built variable current source. In this work, two different irradiation spectra were employed to simulate solar radiation: AM1, representing ground-level sunlight after atmospheric filtering, and AMO, representing sunlight before absorption by the atmosphere, including wavelengths below 300 nm. Additionally, individual wavelengths (280, 310, 345, 365, 385, 405, 430, 470, 490, and 520 nm) as well as the UV portion of the AM0 spectrum were employed. Additional technical details, including LED spatial distribution, irradiation spectra of AM0 and AM1, and homogeneity calibration, are provided in the Supplement. The irradiation cell was placed on a large metal table that served as an effective heat sink, inside a well temperature-controlled room. A quartz window allowed light to pass through for irradiation. The LED light source emitted at wavelengths below 550 nm and produced no thermal radiation. Cooling air from the light source electronics was vented away from the measurement cell.

2.3 SFG spectroscopy

Surface sum-frequency generation (SFG) spectroscopy is based on a second-order nonlinear optical effect that in dipole approximation only occurs where the inversion symmetry is broken, which is always the case at interfaces between two phases (Miranda and Shen, 1999; Zhang et al., 1994). SFG is generated by a temporal and spatial overlap of two different frequency light pulses (usually visible and a tunable IR) at

an interface between two isotropic media. It provides information about the interface by probing the individual species from their IR vibrational absorption (Shen, 1989). SFG has proven effective in probing aqueous solutions containing soluble ionic and molecular species and in determining the role of these substances in changing the water structure at the interface (Schultz et al., 2002; Shultz et al., 2000). Surfactants partition to the interface and can displace or bind water into hydrated complexes. Various SFG investigations on air—water interfaces have centered on examining organic surfactants adsorbed at the water surface (Backus et al., 2012; Doughty et al., 2016; Ghosh et al., 2009; Henry et al., 2003; Rao et al., 2011; Truong et al., 2019; Varga et al., 2005). However, it is mandatory to focus on studies that include atmospherically relevant substances under atmospheric conditions.

The description of the SFG spectrometer used in this study can be found elsewhere (García Rey et al., 2019). The irradiation and ray geometry used in the present work are shown in Fig. S3. Details of the SFG experiments and data analysis can be found in the Supplement (Sect. S3). The individual bands fitted to the different species are shown in Fig. S7. Table S2 lists the experimental conditions of all SFG experiments conducted in this work. At first glance, due to the distinguished feature of SFG as a sub-monolayer surfacesensitive technique, we realized that the delivered 4-BBA contained surface-active contaminants. The purple spectrum in Fig. S6 shows vibrational bands in the CH region detected at the surface of a 0.2 mM aqueous solution of 4-BBA. These bands are attributed to surface-active organic contaminants in the solution. 4-BBA is not surface active (Mora Garcia et al., 2021), and there are no free CH bonds that could produce the CH vibrations. To purify the 4-BBA, it was recrystallized twice from ethanol. The green curve in Fig. S6 shows the SFG spectrum of 4-BBA aquatic solution after the recrystallization. It is worth mentioning that we tested samples from different providers, including the provider mentioned in the reference work (Tinel et al., 2016), and found that 4-BBA was never delivered pure enough to not show surface-active contaminants. The contamination in the 4-BBA should be considered when comparing our results with those in the reference work.

2.4 Mass spectrometry

The analysis of liquid-phase products was carried out using the Filter Inlet for Gas and Aerosols (FIGAERO, Aerodyne Inc.) in combination with a high-resolution time-of-flight chemical ionization mass spectrometer (HR-ToF-CIMS, Aerodyne Inc.), employing I^- as the ionization reagent. A 2.5 μL liquid sample was applied to a PTFE filter via a syringe and subsequently subjected to thermal desorption in FIGAERO-CIMS. To ensure that the sampled liquid solution was representative of the entire system, the solution was thoroughly stirred prior to sampling to homogenize any

surface-enriched compounds with the bulk. The syringe tip was then inserted into the center of the bulk phase to draw the sample. Ultra-high-purity nitrogen served as the carrier gas, facilitating desorption as the temperature was gradually increased from 296 K to a peak of 473 K over 35 min. The total liquid-phase signal for each compound was determined by integrating its thermal desorption profile (thermogram). Data processing was performed using Tofware v3.1.2, with massto-charge ratios adjusted by subtracting the reagent ion I⁻. To enable comparisons, all ion signals were normalized to 10⁶ cps I[−]. A proton-transfer-reaction time-of-flight mass spectrometer (PTR-ToF-MS 4000, Ionicon Analytic GmbH) was utilized to measure the concentrations of gas-phase compounds. The data were analyzed by PTR viewer 3.3.12. The gas phase was sampled by a syringe and transferred to the PTR-MS. Table S3 lists the experimental conditions of all MS experiments conducted in this work. Since the photoreactor cannot be considered completely air-tight, the measured concentrations cannot be converted into absolute yields of the gas-phase reaction products. Results of the mass spectrometry given in the "Results and discussion" section were subtracted by the background signals measured in the reference experiment MS_BG1.

The choice of analytical instrumentation significantly impacts the range and type of compounds detected in complex samples. In the reference work by Tinel et al. (2016), after PFBHA derivatization, the use of reversed-phase ultra-performance liquid chromatography coupled to high-resolution mass spectrometry (UPLC/(±)HESI-HRMS) allowed for the separation and detection of a broad range of compounds from the aqueous phase. The FIGAERO-CIMS employed in this study is particularly well-suited for the detection of semi-volatile to low-volatility organic compounds, especially for organic compounds with three or more oxygen atoms (Riva et al., 2019). Thus, the two techniques offer complementary insights, with UPLC-HRMS capturing a wider polarity range of dissolved species and FIGAERO-CIMS covering products with higher O/C ratios.

3 Results and discussion

3.1 SFG at the air-liquid interface

Figure 1 shows the SFG spectra at the air–water interface for NA (Fig. 1a), and 4-BBA (Fig. 1b), in dark conditions and after exposure to AM0 light. AM0 was chosen because it includes the maximum portion of sun UV that can lead to photo-induced chemistry in the atmosphere. The solution's pH was first adjusted to pH 8, which is the approximate pH value of the ocean (Jiang et al., 2019). Appropriate data fitting of the SFG spectrum of NA in dark conditions (black curve Fig. 1a) shows vibrational broad OH bands from hydrogen-bonded interfacial water centered at ~ 3450 and $\sim 3250 \, \mathrm{cm}^{-1}$ and narrow CH bands (CH₃ Fermi peak at 2946 cm⁻¹, CH₂ Fermi peak at 2917 cm⁻¹, CH₃

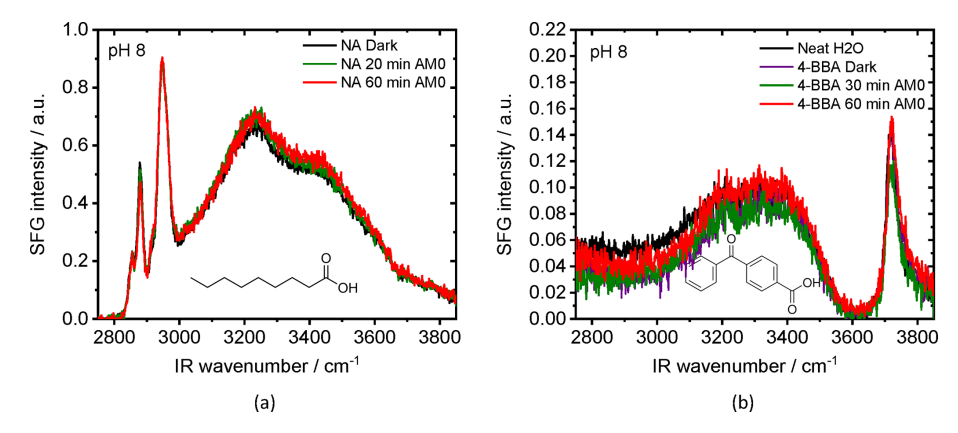


Figure 1. SFG at (a) air—water interface for NA (2 mM) and (b) 4-BBA (0.2 mM) as a function of time in dark conditions and after exposure to AM0 light. Both solutions were adjusted to pH 8.

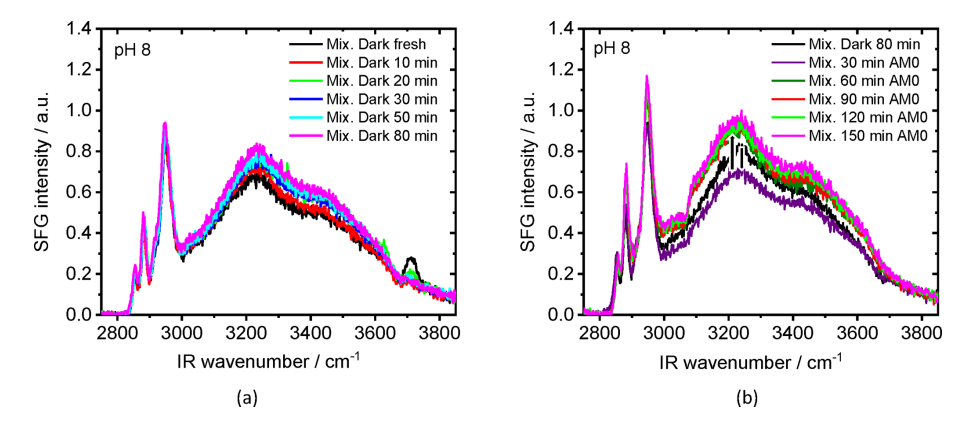


Figure 2. Changes of SFG spectra at air—water interface of a 2 mM NA mixture with 0.2 mM 4-BBA at pH 8 as a function of time under (a) dark conditions as well as for (b) irradiation with AM0.

symmetric-stretch 2885 cm⁻¹, and CH₂ symmetric-stretch at 2858 cm⁻¹) (Lu et al., 2005; MacPhail et al., 1984; Snyder et al., 1982). The CH₂ Fermi resonance appears as a shoulder next to the CH₃ Fermi peak and could be identified by the SFG data fitting as shown in the Supplement. The so-called dangling OH band (~3700 cm⁻¹), which characterizes neat air—water interfaces and arises from water molecules with one non-hydrogen-bonded OH group pointing into the vapor phase (Sovago et al., 2008), was not detected in Fig. 1a. This indicates full coverage of the water surface by NA. The dark SFG spectrum of 4-BBA (purple curve Fig. 1b) shows an SFG spectrum very similar to that of the neat air—water interface (black curve Fig. 1b). There are no noticeable signs of 4-BBA at the interface, as expected, since 4-BBA is not surface-active.

As shown in the SFG spectra in Fig. 1a, AM0 irradiation of the NA solution without 4-BBA produced no detectable changes in the SFG signal, indicating negligible photoreactivity in the absence of 4-BBA. In contrast, Fig. 1b shows that while the OH stretching modes of hydrogen-bonded interfacial water (~ 3250 and $\sim 3450\,\mathrm{cm}^{-1}$) remain within the signal-to-noise range upon AM0 irradiation of 4-BBA alone,

a decrease in the dangling OH band ($\sim 3700\,\mathrm{cm}^{-1}$) is observed after 30 min of exposure (green curve) compared to the dark signal (blue curve). Interestingly, after 1 h of irradiation, the dangling OH signal (red curve) returns to its initial intensity, matching the dark signal. Although subtle, these variations in the SFG signal suggest perturbations in interfacial water structure, possibly due to the formation of photoproducts.

Figure 2a shows the SFG spectra from air-water interfaces for mixtures of NA and 4-BBA at a solution pH 8 as a function of time after which the interface was established, while the samples were continuously kept in the dark conditions (no light exposure). There is a visible change in the signal along the whole frequency range. Close inspection of Fig. 2a reveals that the dangling OH band decreased with time to negligible intensity after ~ 50 min under dark conditions. We have fitted the dangling OH band at different times and present the results in Fig. S8, which clearly shows the decay of dangling OH intensity as a function of time. These changes reflect the adsorption rate and structuring of NA at the air-water interface at pH 8, which are accompanied by a slight increase in the OH bands at ~ 3450 and ~ 3250 cm⁻¹

from interfacial water (Figs. 2a and S9), indicating a relatively slow restructuring of water molecules at the interface. At the same time, the CH₃ symmetric-stretch peak intensity, which we assume to be proportional to the number of interfacial NA, slightly increases with time when the sample was kept in the dark (see Fig. S10). The small increase in the CH bands is expected due to ongoing interface adsorption until equilibrium is reached with full surface coverage and is not expected to be caused by photochemistry as all the experiments with the mixture so far were performed under dark conditions. Although it was confirmed that 4-BBA partitions to the surface in the presence of NA (Tinel et al., 2016), no significant spectral signature of 4-BBA is observed at the air-mixture interface. Only a very weak narrow band at $\sim 3070 \,\mathrm{cm}^{-1}$, which can be ascribed to a =C-H stretch in an aromatic compound (Gautam et al., 2000; Hardt et al., 2024), could be identified after the data fitting of the dark spectrum of the mixture (Fig. S11a for pH 8 and Fig. S11c for pH 5.4). We attribute this negligible contribution to the dominant presence of NA forming the top layer, hindering the 4-BBA from directly interfacing with air, limiting its contribution to surface signal, particularly since 4-BBA itself is not inherently surface-active.

Figure 2b shows SFG spectra at air—water interface for the mixture at pH 8, which was first equilibrated for 80 min in dark and then exposed for different times to AM0 irradiation. There are two observed phenomena: (1) a significant increase in the aromatic band at 3070 cm⁻¹ as identified from the data fitting (Fig. S11b, Gautam et al., 2000; Hardt et al., 2024) and (2) a bidirectional change, decrease, and then increase in the peak intensity of the water bands as identified directly from the spectra. The latter means that two opposing processes occur simultaneously at the interface. The appearance of the new band is expected and can be attributed to the photochemistry taking place at the water surface.

One possible reason for the bidirectional amplitude changes of the water bands under light conditions, as well as the slight change under dark conditions, is the change of pH of the bulk solution. Indeed, we found that the pH decreases with time for the same mixture under dark and light (UV) conditions until the pH stabilizes around a neutral pH (Fig. S13a). Under dark conditions, the solution's pH decreases exponentially with time; however, under irradiation conditions, the pH also decreases but with a higher rate (blue curve in Fig. S13a). The decrease in pH under dark conditions is due to the carbonation of the solution under room conditions as was observed for a pH 8 solution without the mixture (orange curve Fig. S13a). The enhanced decrease in pH upon UV irradiation is only observed at pH 8 of the mixture solution which indicates a contribution from the reaction products. On the one side, the water molecules at the surface are directly affected by the surface charge (Nihonyanagi et al., 2013). On the other side, the change in bulk pH changes the dissociation fraction of NA (Fig. S13b) and accordingly its concentration at the surface, which in turn indirectly affects the water structuring and hence the SFG signal. The influence of pH on the detected SFG signal is described in details in the Supplement (Sect. S4).

To eliminate the complexity of the pH effect and to reduce the number of variables, we examined the same system but at a slightly lower pH value (pH = 5.5 ± 0.1), which is not sensitive to carbonation and other factors that may change the pH value over time (green curve Fig. S13a). Indeed, the behavior of water bands (increase under dark conditions and decrease and then increase under light conditions) was not observed for low pH solution, Fig. 3b. In addition, the dangling OH, which characterizes the neat air-water interface, was not observed at low pH in the first dark measurement, Fig. 3a. This means that the spread of NA on the surface was faster than that in the case of high pH. This is in line with the dependency of the dissociation constant of NA on pH. At intermediate pH, a considerable portion of negatively charged molecules are neutralized to create neutral fatty acid molecules, which have a much greater adsorption constant than their anionic counterparts (Badban et al., 2017). The aromatic CH stretching band at $\sim 3070 \, \mathrm{cm}^{-1}$ was visible in the SFG spectrum after 60 min, which is about the same time when it appeared for solution with pH 8 (Fig. 2b). However, the data fitting shows that the aromatic band, for both pH values, started to increase directly after starting irradiations

The slight changes in the CH bands (2800–3000 cm⁻¹ region) in Fig. 3b indicate variations of the chemical composition in the topmost layer at the air-water interface. The significant increase in the aromatic band ($\sim 3070 \,\mathrm{cm}^{-1}$) indicates the formation of surface-active aromatic compound(s). The OH stretching modes in the 3100–3500 cm⁻¹ region, associated with interfacial water, increased after irradiation with AM0 (see the fitted spectra in Fig. S11). There is a clear proportion between the increase in the water band and the aromatic band (Fig. 4a). We attribute this to the formation of amphipathic aromatic compounds after irradiation, which can alter the hydrogen-bonding structure of water at the interface. Since SFG spectroscopy is inherently sensitive to the net polar orientation of interfacial molecules detecting vibrational modes only when molecular ordering breaks inversion symmetry, an increase in the SFG signal of hydrogenbonded OH stretches indicates that water molecules at the interface have adopted a more ordered, non-centrosymmetric arrangement. This provides evidence for the presence of amphipathic species at the air-water interface, which promote directional hydrogen bonding via their polar headgroups. As a result, interfacial water molecules become more aligned, breaking the random symmetry of bulk water, orienting OH dipoles, and enhancing the net polar order, manifested as an increased SFG signal in the OH stretching region (Gragson and Richmond, 1998; Kusaka et al., 2018). A direct comparison between the fitted amplitudes of the aromatic band $(\sim 3070 \,\mathrm{cm}^{-1})$ for pH 5.4 and pH 8 mixtures (Fig. 4b) shows a greater relative increase at pH 5.4, indicating a more fa-

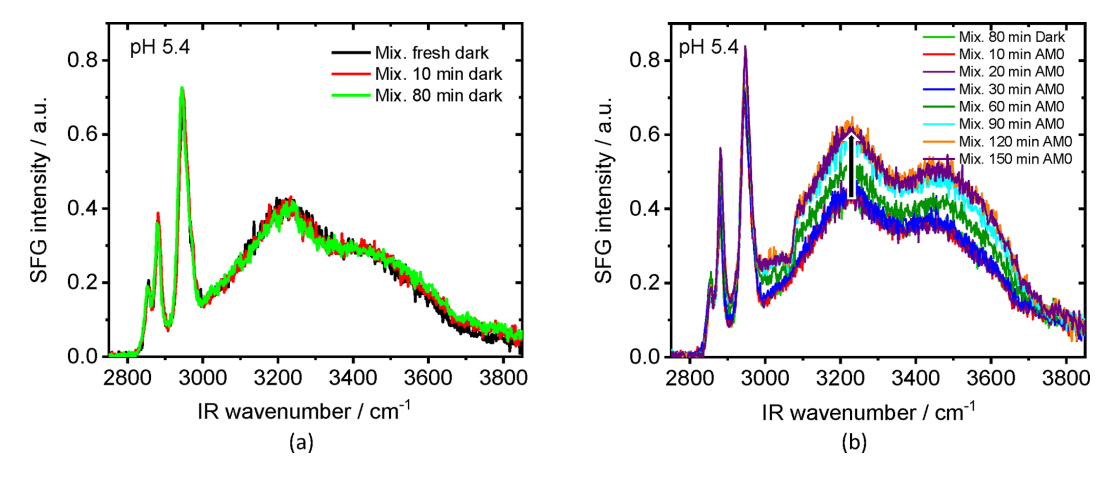


Figure 3. SFG spectra at air—water interface of the mixture (2 mM NA + 0.2 mM 4-BBA) at pH 5.4, under dark conditions (a) and irradiation with AM0 (b) conditions.

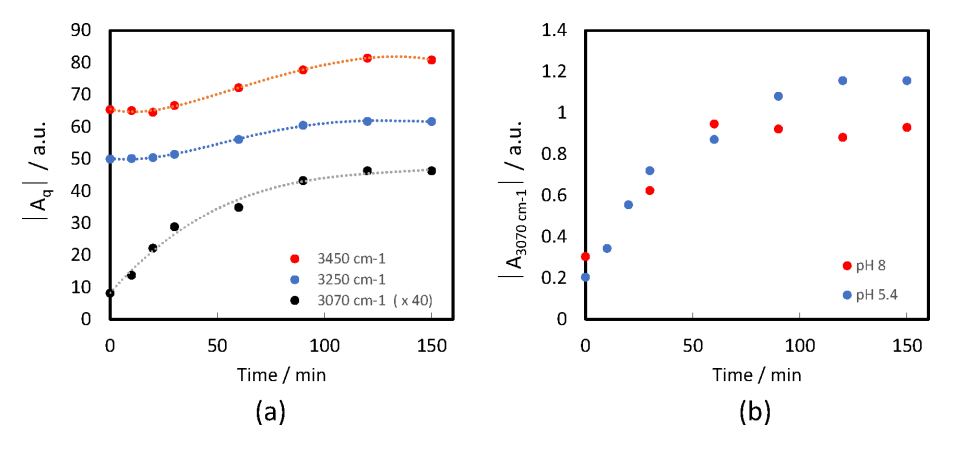


Figure 4. Time-dependent changes in the fitted SFG peak amplitudes with AM0 irradiation. (a) The aromatic band ($\sim 3070 \, \mathrm{cm}^{-1}$) and the two water bands ($\sim 3250 \, \mathrm{and} \sim 3450 \, \mathrm{cm}^{-1}$) for the mixture at pH 5.4 (dashed lines are included as visual guides). (b) The aromatic band ($\sim 3070 \, \mathrm{cm}^{-1}$) for the mixtures at pH 5.4 and pH 8.

vorable environment for the formation of the corresponding amphipathic aromatic compound. We attribute this tendency to the excess of hydrogen ions at lower pH, which can be abstracted by the photoexcited 4-BBA resulting in the formation of $C_{14}H_{11}O_3^{\bullet}$ radical in the solution (Reaction R1). This radical plays an important role in the consequent reactions shown in the "Tentative reaction pathways" section (Sect. 3.2.3).

The real solar radiation spectrum depends on weather, latitude, altitude, and season. These factors qualitatively and quantitatively affect the photochemistry in the hydrosphere. In Fig. 5, we compare the effect of three irradiation conditions; AM0, AM1, and solely the UV portion ($\lambda < 400\,\mathrm{nm}$) of AM0 for 90 min on the same mixture. The SFG spectra show strong variations after continuous irradiation with AM0 for 90 min (Fig. 5a). In contrast, the solution exposed to AM1 shows little presence of an aromatic band and a slight increase in water bands after the same irradiation time (Fig. 5b), which is in line with the reduced intensities of all

spectral wavelengths, particularly the UV portion. Irradiating the mixture with only the UV portion of AM0 ($\lambda < 400\,\text{nm}$) shows a clear aromatic band with minimal changes in the water bands (Fig. 5c). This provides evidence that the UV contribution plays a primary role in the formation of the surfaceactive aromatic compounds. Consequently, this photoreaction is likely more pronounced in the atmosphere (e.g., in cloud droplets) than at the sea surface where the UV intensity below 300 nm is very weak (see Fig. S4).

Solutions at pH 5.6 were irradiated by 10 different wavelengths for the same time (18 h), and an SFG spectrum was collected for the fresh solution, then after 0.5, 3, and 18 h of irradiation time. Each irradiation wavelength was individually adjusted to match the corresponding intensity in the AM0 solar spectrum, so that in separate irradiation experiments, each wavelength independently reflected its relative contribution to the AM0 spectral power. The SFG spectra are shown in Figs. 6 and S12. Both figures correspond to the same set of measurements but with different display for-

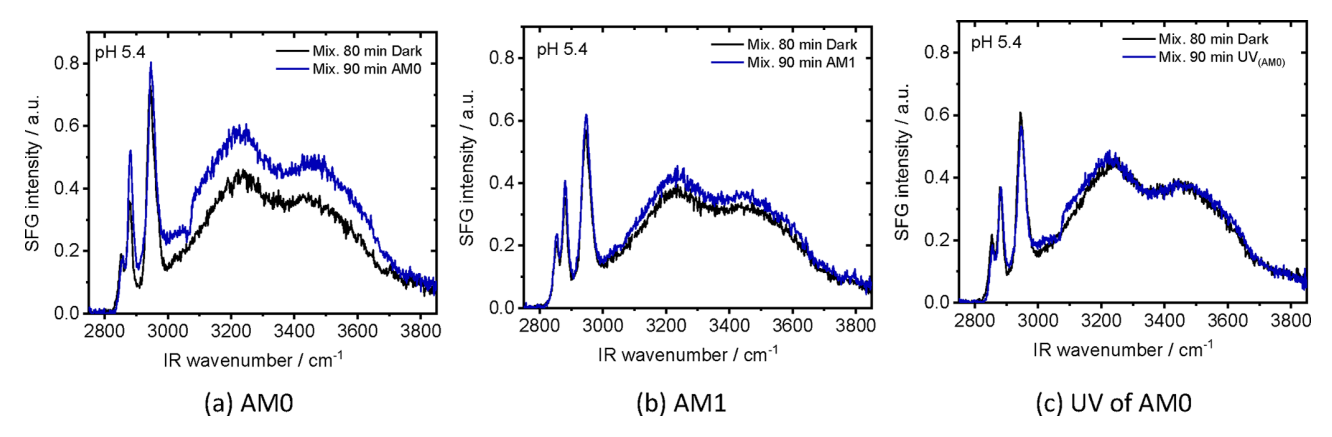


Figure 5. SFG spectra at air—water interface of 2 mM NA aqueous mixtures with 0.2 mM 4-BBA at a pH of 5.4, before and after irradiation with (a) AM0, (b) AM1 and (c) UV portion of AM0.

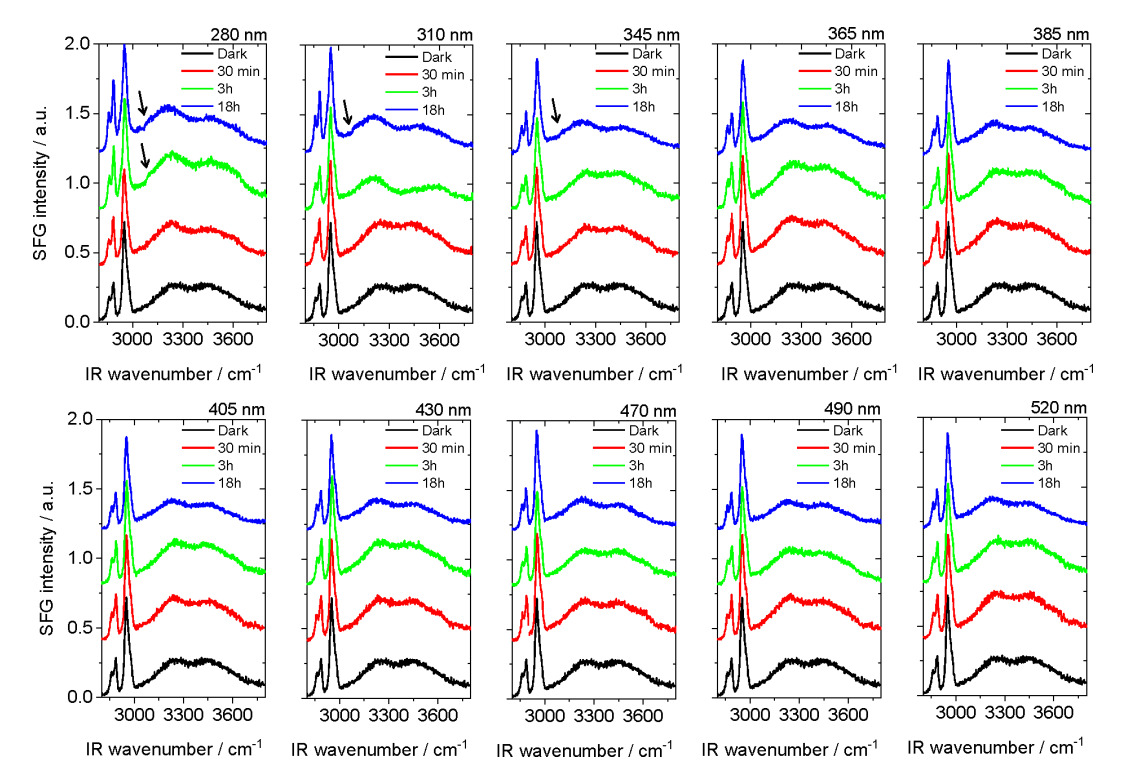


Figure 6. SFG spectra at air—water interfaces of (2 mM NA + 0.2 mM 4-BBA) mixtures at pH 5.6 after different times of irradiation with different wavelengths. Note that the spectra have a constant with offset.

mats to illustrate the change in the aromatic band and the changes in water bands, respectively. Figure 6 shows that the aromatic band was considerably visible in the SFG spectrum and without data fitting (see black arrows) only in the short UV wavelengths, mainly 280, 310, and 345 nm, confirming the responsibility of the UV portion of the light for the generation of the aromatic compound(s). The effect of different wavelengths has different weights due to the changes in intensity and wavelength simultaneously. The shorter wavelength and/or higher intensity has a stronger effect on both

the surface-active and bulk species. For the sample irradiated by 280 nm, the aromatic band was visible already after 3 h, although it has the lowest intensity in the irradiation spectrum. Figure S12 shows that the water bands were changing differently with different wavelengths. In most of cases, the change in the aromatic CH stretching band was stronger at shorter wavelengths. The solution irradiated with 365 nm shows a change in the water band after 3 h, similar to that of the solution irradiated with 280 nm. Except for the 310 nm, there is always an increase or negligible change

in the water bands after 3h of irradiation. Except for 280 and 310 nm, the water bands after 18h of irradiation showed a minimum. These variations in the water bands indicate changes in the hydrogen bonding structure at the interface due to the composition and abundance of the different photoproducts with different irradiations. The results highlight the complex impact of solar spectrum composition on reaction pathways. They also emphasize the importance of incorporating these variations into the photochemical models used in atmospheric science for more accurate predictions of the complex chemical interactions that occur in the atmosphere (Xing et al., 2022).

Finally, although it is not intended to investigate the salinity effect on the photochemistry at the surface in this study, we report on its potential influence on the photoreaction of the NA-4BBA system. A SFG pilot experiment showed that the salt concentration of the bulk accelerates the photoreaction (see Sect. S5 and Fig. S15). We only register the observed phenomenon and aim at detailed study in future work.

3.2 Organic compounds in liquid and gas phase

The aromatic compound detected at the air—water interface by SFG spectroscopy is a result of a photoreaction occurring for the studied samples when they are irradiated with UV containing radiation, e.g., AM0. The reactions in the visible wavelength range were neither expected nor previously reported. Considering these facts and recalling that the mass spectroscopic results in Tinel et al. (2016), although very thorough, were collected from samples irradiated with a commercial Xenon lamp as a light source, and that the 4-BBA sample was not purified as ours, we decided to repeat the mass spectrometry measurements using our solar simulator and purified 4-BBA samples (see the "Experimental procedures" section (Sect. 2)).

3.2.1 Aqueous-phase analysis

The products of the photochemical reactions of NA in the presence of 4-BBA were detected under different irradiation and at a fixed pH of \sim 5.8. Figure 7 shows the evolution of seven main liquid-phase products detected in experiment MS.1 under irradiation with AM0 and in the presence of 4-BBA as photosensitizer with the following sum formulas: $C_8H_{12}O_4$, $C_8H_{12}O_5$, $C_9H_{10}O_5$, $C_9H_{14}O_3$, $C_9H_{16}O_3$, C₉H₁₆O₄, and C₁₀H₁₄O₄. Among the photoproducts identified in the liquid phase, only C₉H₁₆O₃ and C₉H₁₆O₄ were also reported in the reference study (see Table S4). Conversely, the reference study reported additional products that were not detected in our analysis (see Table S6). This could be attributed to the purity of the sample, the spectral intensity distribution of the light source, and/or the different analytical instrumentation, as mentioned in the "Experimental procedures" section (Sect. 2). The suggested assignments of the detected compounds in the liquid phase are listed in Table S4.

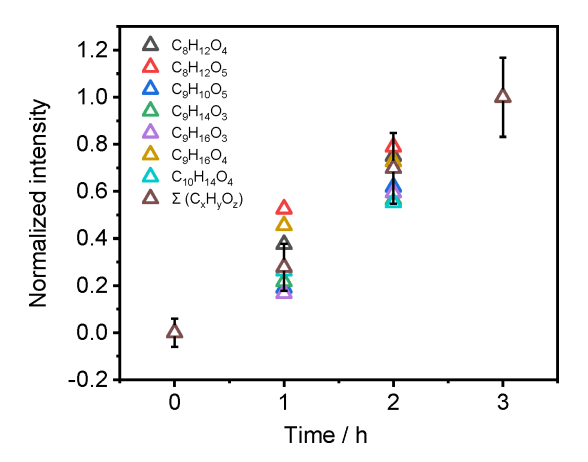


Figure 7. Intensities of individual photoproducts as a function of exposure time to AM0 irradiation (Exp. MS.1), normalized to the total liquid-phase signal intensity Σ ($C_xH_yO_z$). Error bars represent the uncertainty associated with the analytical measurements.

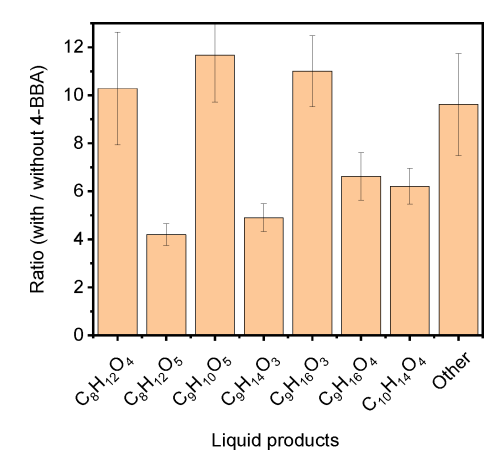


Figure 8. Ratio of the signal detected in the presence of 4-BBA to that without 4-BBA for the main photoproducts detected in the aqueous phase of NA solution irradiated with AM0 for 3 h in a synthetic air environment.

Some of the products showed faster production rates during the first hour, while the others showed a slower rate. We do not observe any correlation between the production rate and chain length, nor the molecular weight. However, the differences are close to the experimental uncertainties. The sum of all $C_xH_yO_z$ signal intensities in the liquid phase shows a linear relation with the time of irradiation (Fig. 7). Figure 8 shows the ratio of signals detected for the main liquid-phase photoproducts of the mixture (NA + 4-BBA) versus the signals detected in the absence of 4-BBA with irradiation of AM0 and in the presence of synthetic air. The results show the largest promotion in the formation of $C_8H_{12}O_4$, $C_9H_{10}O_5$, and $C_9H_{16}O_3$ in the presence of 4-BBA.

To examine the role of oxygen in the reactions, we repeated the AM0 experiment with pure nitrogen, instead of the synthetic air, and deoxygenated liquid solutions (Exp.

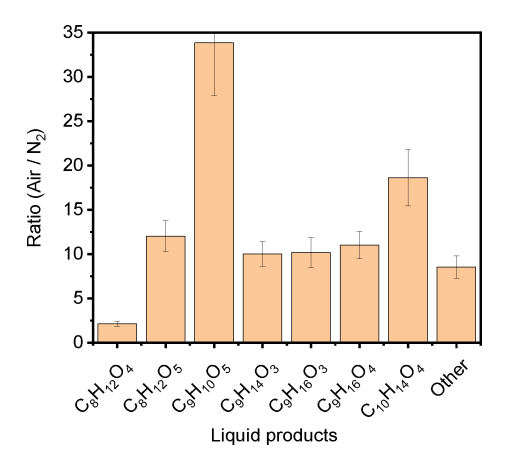


Figure 9. Ratio of the signal detected in the synthetic air environment to that in the absence of oxygen in gas and liquid phase for the main photoproducts detected in the aqueous phase of NA with 4-BBA, after irradiation with AM0 for 3 h.

MS.3). The solution was deoxygenated by bubbling with nitrogen for 10 min, and the measuring cell was purged before closing it hermetically. Figure 9 shows the ratio of signals detected in the presence of synthetic air versus those in the presence of N_2 . The results show that the presence of oxygen causes an increase in $C_8H_{12}O_5,\ C_9H_{14}O_3,\ C_9H_{16}O_3,$ and $C_9H_{16}O_4$ by a factor of 10 to 12. The presence of oxygen shows only a limited promotion on the formation of $C_8H_{12}O_4$ (factor of \sim 2) but a significant promotion on the formation of $C_{10}H_{14}O_4$ (factor of \sim 19) and $C_9H_{10}O_5$ (factor of \sim 34). This emphasizes the vital role of dissolved oxygen in the natural bodies of water to develop multiple pathways of interactions.

The SFG spectra of solutions irradiated with different single wavelengths (Fig. 6) exhibited varying changes in the water bands regardless of the appearance of the aromatic CH stretching band. To quantify the effect of different irradiation wavelengths on the generation of photoproducts, we further examined the solution mixture irradiated with four selected single wavelengths in the UV and visible part of the spectrum (Exp. MS.4 - 285 nm, MS.5 - 310 nm, MS.6 - 365 nm, and MS.7 – 405 nm) and also with sunlight during a clear sunny day in Karlsruhe, Germany, on 1 June 2023 from 11 am to 2 pm central European summer time (CEST; UTC+2) (Exp. MS.8). The day and time in the sunlight experiment were chosen to guarantee minimal changes in the solar radiation spectrum. Figure 10 shows the total $C_x H_y O_z$ signal detected in the liquid phase for different irradiation conditions, as illustrated on the x axis. As can be inferred from Fig. 10, with stronger UV light at AMO, the formation of major aqueous photoproducts was promoted, with the increase in total $C_x H_y O_z$ signal by a factor of about 2.4 compared to that at AM1. After being irradiated by real solar light for 3 h, the total $C_x H_y O_z$ signal observed was ~ 0.9 of that observed at AM1. Hence, our experiments with AM1 irradiation are in-

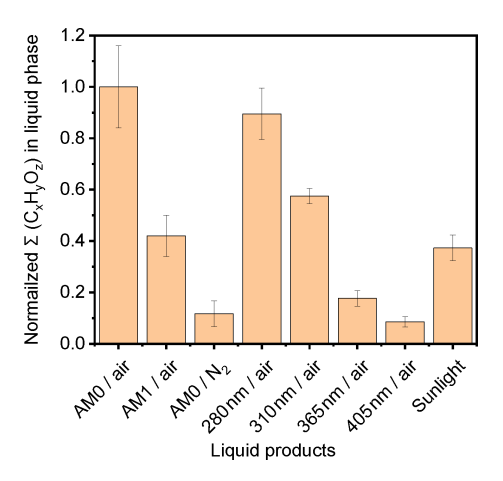


Figure 10. Normalized total $C_xH_yO_z$ signal in aqueous phase at different irradiation conditions for 3 h (Exps. MS.1 to MS.9 in the Supplement).

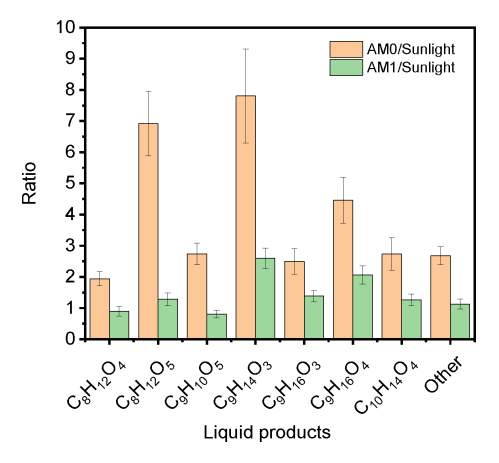


Figure 11. Ratio of the compounds detected with AM0 or AM1 versus the signal with sunlight, for a NA aqueous solution with 4-BBA after irradiation for 3 h.

deed comparable to typical atmospheric conditions at earth surface. Figure 11 shows a comparison between the ratios of the photoproducts for the mixtures irradiated with AMO (Exp. MS.1) and with AM1 (Exp. MS.2) versus irradiation with real sunlight (Exp. MS.8). The same main set of photoproducts observed under artificial irradiation in the laboratory were also detected under sunlight. The relative product fractions for irradiation with sunlight are very similar to those of the lab irradiation and mostly lie between those of irradiation by AM0 and AM1. The fractions of the photoproducts that constitute 2 % or more of the total products under real sunlight (i.e., $C_9H_{16}O_4$, $C_{10}H_{14}O_4$, $C_8H_{12}O_4$, $C_9H_{16}O_3$, and C₉H₁₀O₅, in order of ascending fraction) are closer to those of AM1, which is consistent and emphasizes the capability of our homemade light source to simulate ambient solar radiation.

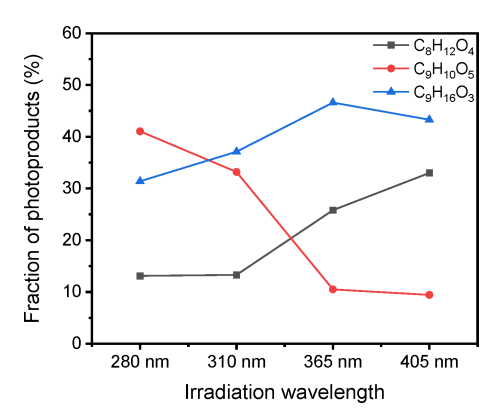


Figure 12. The fraction of photoproducts versus wavelength for the three most dominating products $(C_8H_{12}O_4, C_9H_{10}O_5, \text{ and } C_9H_{16}O_3)$ in a NA aqueous solution with 4-BBA after irradiation with 280, 310, 365, and 405 nm for 3 h.

To address the wavelength dependence of the photoproducts further, we plot the fraction of the three most dominating products, namely $C_8H_{12}O_4$, $C_9H_{10}O_5$, and $C_9H_{16}O_3$, versus irradiation wavelength in Fig. 12. The fractions of $C_8H_{12}O_4$ and $C_9H_{16}O_3$ increase with longer wavelength, while the fraction of the $C_9H_{10}O_5$ increases with shorter wavelength, indicating two different mechanisms, as will be described below.

In all MS experiments, $C_8H_{12}O_4$, $C_9H_{10}O_5$, and $C_9H_{16}O_3$ were the most abundant products detected in the liquid phase. However, the fractions of the liquid-phase compounds varied under different irradiation conditions (Fig. 13a-h). The C₈H₁₂O₄ is a major product from the photoreaction of NA with limited dependence on oxygen compared to other products. This is evident from the relative increase in C₈H₁₂O₄ in total liquid-phase products during the experiment with pure nitrogen (Fig. 13c), where it becomes the main product, despite a much lower overall production. The formation of C₈H₁₂O₄ was also significantly increased in the presence of 4-BBA (Fig. 8), indicating that C₈H₁₂O₄ was a photodegradation product from NA in the presence of 4-BBA. For C₉H₁₆O₃, which is suggested to form through RO₂ radical reactions after hydrogen abstraction (Tinel et al., 2016), its fraction of total liquid-phase $C_x H_y O_z$ was higher with irradiation of AM1 than AM0 (Fig. 13b and a). This stands in agreement with the measurement with irradiation from 280 nm to 405 nm (Fig. 13e-h). With more UV at 280 and 310 nm, $C_9H_{16}O_3$ accounted for about $\sim 31\%$ and $\sim 37\%$ of total $C_x H_y O_z$, respectively, while with less UV at 365 and 405 nm, the fractions of $C_9H_{16}O_3$ increased to $\sim 47\%$ and \sim 43 %, respectively. In previous work by Tinel et al. (2016), the solution with NA and 4-BBA showed that the formation of $C_9H_{16}O_3$ increased by a factor of ~ 2.5 in the presence of air. In our study, with 4-BBA the formation of C₉H₁₆O₃ increased by a factor of ~ 11 . The oxygenated C₉ products are promoted when O₂ is abundant, which agrees with Tinel et al.

(2016). In contrast to $C_8H_{12}O_4$ and $C_9H_{16}O_3$, the fraction of $C_9H_{10}O_5$ in total liquid-phase $C_xH_yO_z$ decreased from \sim 41 % at 280 nm to \sim 9 % at 405 nm and also from \sim 34 % at AM0 to \sim 24 % at AM1. We observed a higher fraction of $C_9H_{10}O_5$ in experiments involving NA and 4-BBA under enhanced UV conditions, suggesting that $C_9H_{10}O_5$ is likely an aromatic compound formed through reactions between photoproducts generated from the photolysis of both NA and 4-BBA. This interpretation aligns with the presence of two distinct reaction mechanisms, as inferred from Fig. 12, where 4-BBA functions both as a photosensitizer for NA, producing nonaromatic products such as $C_8H_{12}O_4$ and $C_9H_{16}O_3$, and as a photolabile compound that yields aromatic photoproducts that may undergo further reactions.

3.2.2 Gas-phase analysis

Examining the gas phase is important to detect volatile photoproducts. A series of compounds, such as C_4H_8 (butene), C_4H_8O (butanal), C_5H_{10} (pentene), $C_5H_{10}O$ (pentanal), C_6H_6 (benzene), C_7H_8 (toluene), C_7H_6O (benzaldehyde), and $C_8H_{16}O$ (octanal), as well as some undefined fragments such as C_6H_5 and C_7H_6 were detected in the gas phase (see Table S5). Similar to the liquid phase, only a subset of the photoproducts identified in the gas phase, namely C_4H_8 , C_4H_8O , C_5H_{10} , $C_5H_{10}O$, and $C_8H_{16}O$, were also reported in the reference study, which, in contrast, identified additional products not observed in our analysis (see Table S6).

Only two of the photoproducts detected in the gas phase showed a significant increase compared to the background experiments (BG1-3). Figure 14 shows the normalized signals of the two main gas-phase compounds, benzene (C_6H_6) and benzaldehyde (C₇H₆O), under different irradiation conditions. When NA was irradiated in the absence of 4-BBA, the signal from both products remained at background levels. However, when either the mixture or 4-BBA alone was irradiated with AM0, both compounds exhibited strong signals. This is a further confirmation that, in addition to the previously reported photosensitized degradation of NA in the presence of 4-BBA as a photosensitizer, 4-BBA itself undergoes photolysis under the influence of the UV portion of the light spectrum. For other gas-phase compounds detected in this study, no significant differences were observed between the irradiation experiments and the background experiments.

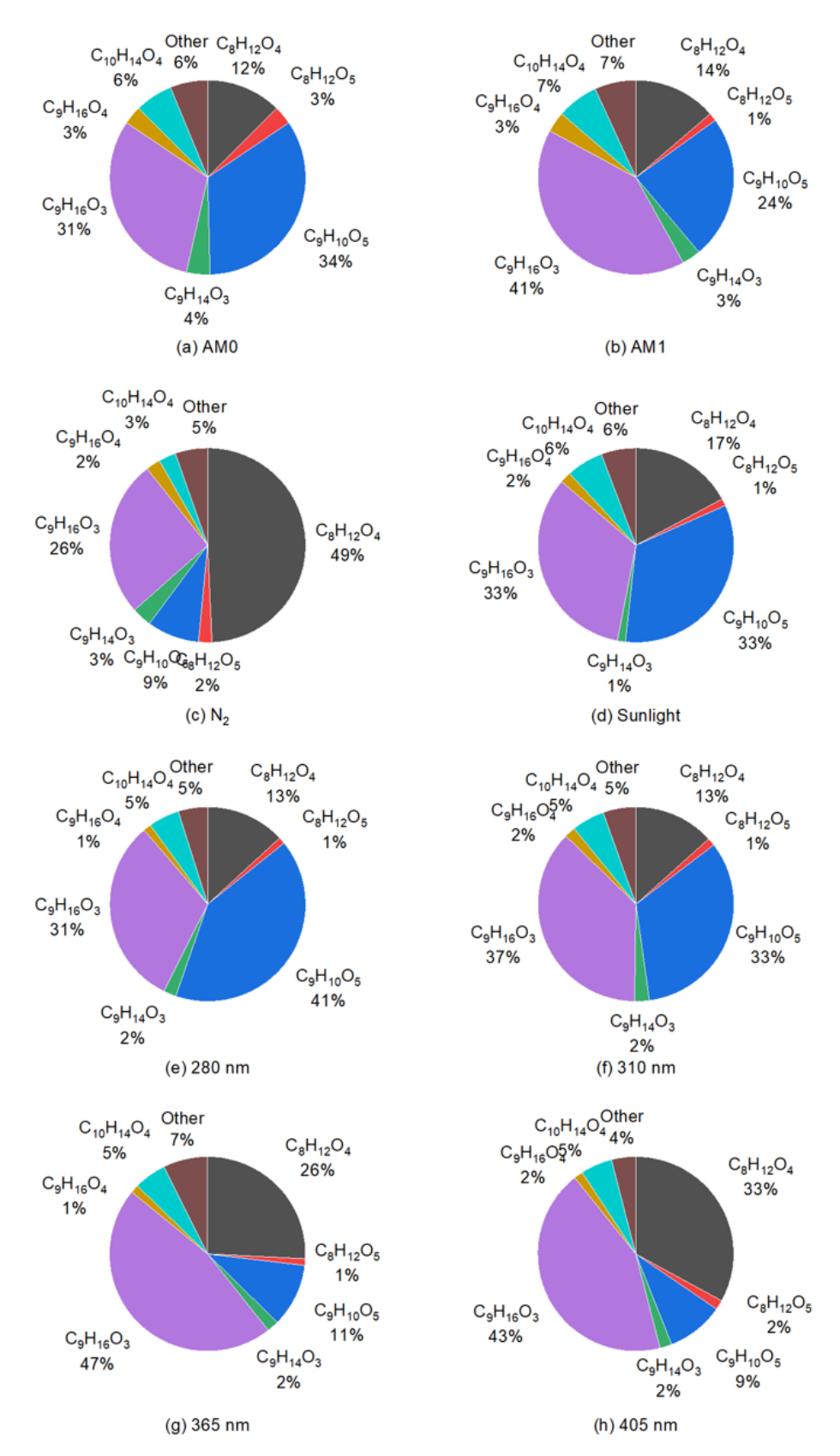


Figure 13. Fractions of products in total liquid-phase $C_x H_y O_z$ under different irradiation conditions. All panels represent experiments conducted in air, except panel (c), which corresponds to an experiment performed in pure nitrogen.

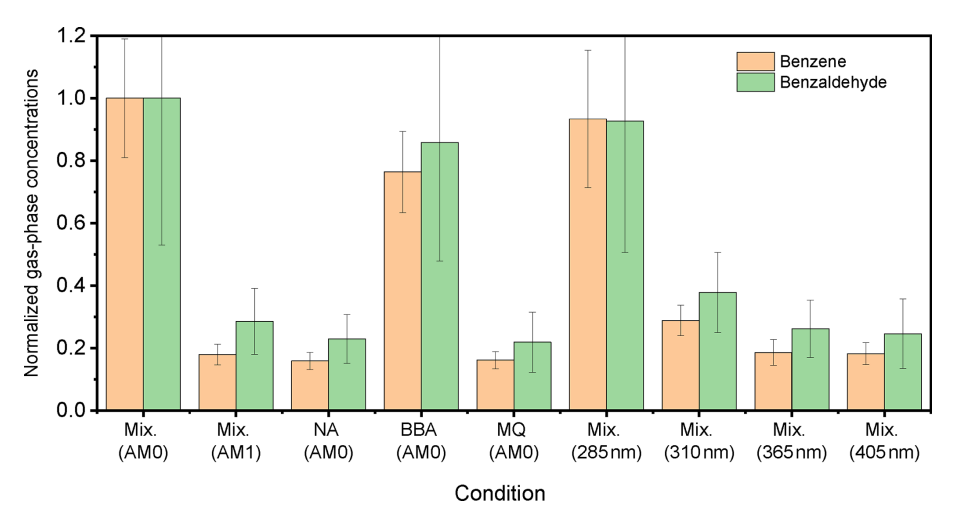


Figure 14. MS signals of benzene and benzaldehyde detected in the gas phase for different solutions under different irradiation conditions for 3 h. Signals are normalized to that of the mixture under AM0 irradiation condition. MQ: Milli-Q water (pH \sim 6.2).

3.2.3 Tentative reaction pathways

The following scheme shows the suggested photolysis of NA in the presence of 4-BBA:

$$4BBA(C_{14}H_{10}O_3) \xrightarrow{hv} 4BBA(C_{14}H_{10}O_3)^*$$

$$4BBA(C_{14}H_{10}O_3)^* + NA(C_9H_{18}O_2)$$
(R1)

$$\xrightarrow{hv} C_{14}H_{11}O_3^{\bullet} + C_9H_{17}O_2^{\bullet}$$
 (R2)

$$C_{14}H_{11}O_3^{\bullet} + H^{\bullet} \xrightarrow{hv \leq 310 \text{ nm}} C_6H_6 + C_8H_5O_3^{\bullet}$$
 (R3)

$$C_9H_{17}O_2^{\bullet} \xrightarrow{O_2} C_9H_{17}O_4^{\bullet} \tag{R4}$$

$$C_9H_{17}O_4^{\bullet} \xrightarrow{RO_2^{\bullet}} C_9H_{16}O_3 + C_9H_{18}O_3$$
 (R5)

$$C_9H_{17}O_4^{\bullet} \stackrel{O_2,HCO_3^{\bullet}}{\longrightarrow} C_{10}H_{14}O_4 \tag{R6}$$

$$C_9H_{17}O_4^{\bullet} + C_{14}H_{11}O_3^{\bullet} \to C_{23}H_{28}O_7$$
 (R7)

$$C_{23}H_{28}O_7 \rightarrow C_9H_{10}O_5 + C_{14}H_{18}O_2$$
 (R8)

$$C_9H_{16}O_3 \xrightarrow{hv,OH} C_9H_{14}O_3 + C_9H_{16}O_4.$$
 (R9)

Bold denotes compounds that have been observed.

The photochemical degradation of NA in the presence of 4-BBA proceeds through a series of radical-mediated reactions. The proposed mechanism begins with the photoexcitation of 4-BBA, generating a reactive triplet state 4-BBA* (Reaction R1) (Dalton et al., 2025), which abstracts a hydrogen atom from either the solvent or NA, generating $C_{14}H_{11}O_3^{\bullet}$ (Jiménez and Miranda, 2018) and forming a NA-derived alkyl radical ($C_9H_{17}O_2^{\bullet}$) (Reaction R2). The $C_{14}H_{11}O_3^{\bullet}$ radical undergoes Norrish I-type cleavage to produce benzene (C_6H_6) and a benzoyl fragment ($C_8H_5O_3^{\bullet}$) with UV absorption at $\lambda \leq 310$ nm (Reaction R3) (Goswami et al., 1985). $C_8H_5O_3^{\bullet}$ may further react with O2 to form oxygenated intermediates. The NA-derived alkyl radical ($C_9H_{17}O_2^{\bullet}$) reacts with oxygen to yield a peroxy

radical (C₉H₁₇O₄) (Reaction R4) (Atkinson, 2000). Subsequent reactions of this peroxy radical include (1) reaction with other RO₂ forming C₉H₁₆O₃ and C₉H₁₈O₃ (Reaction R5) (Freeman-Gallant et al., 2024), (2) oxidation with bicarbonate radicals (HCO₃) (Yan et al., 2019) to form $C_{10}H_{14}O_4$ (Reaction R6), and (3) cross-coupling with the 4-BBA ketyl radical (C₁₄H₁₁O₃•) to produce an unstable adduct (C₂₃H₂₈O₇) (Reaction R7), having a peroxide bond (-O-O-) which is very reactive and unstable under light (You et al., 2020). The unstable C23H28O7 undergoes rapid intramolecular rearrangement and fragmentation. It could fragment into the observed aromatic product C₉H₁₀O₅ and a NA-derived byproduct (C₁₄H₁₈O₂) (Reaction R8). C₉H₁₆O₃ may undergo photooxidation under UV light in the presence of hydroxyl radicals, resulting in the formation of one oxidized product (C₉H₁₆O₄) and one dehydrogenated product (C₉H₁₄O₃), suggesting radical-mediated transformation (Reaction R9) (Numadate et al., 2022). Alternatively, the formation of C₉H₁₆O₄ and C₉H₁₄O₃ could also result from the $RO_2^{\bullet} + RO_2^{\bullet}$ self-reaction (Reaction R5), which requires additional H abstraction from 4-BBA to generate sufficient NAderived radicals. The C₉H₁₀O₅ product, observed in higher concentrations particularly after irradiation with AMO, can be formed in an amphipathic, aromatic, surface-active structure via peroxide intermediates that react with water and give OH radicals (Kroll et al., 2015; Lankone et al., 2020). This product ($C_9H_{10}O_5$) gives rise to the SFG signal at 3070 cm⁻¹ and leads to the increase in the water bands in the region 3100 to 3500 cm⁻¹. Our proposed chemical structures with pathways can be seen in the Supplement, Fig. S16. Compared to the reaction pathways suggested by Tinel et al. (2016), our reactions involve the consequences of the photolysis of 4-BBA under the influence of the UV portion on the irradiation source.

4 Conclusions

This study focuses on the correlation between the photochemical products at the surface and bulk regions. We spotlighted the complex contribution of solar spectral distribution, pH, salinity, and surface photoproducts to the reaction. NA was selected as surfactant and 4-BBA as a photosensitizer, and our combined surface—bulk study was compared to the bulk-phase study by Tinel et al. (2016). Our analysis revealed several photoproducts in both the gas and liquid phases that were not reported in the reference study, while conversely, the reference study identified additional products not detected in our work. We attribute these differences to differences in the analytical techniques used, sample purity, sample volume, duration of irradiation, and the spectral characteristics of the light sources applied.

The SFG technique enabled us to detect and confirm the partition of the non-surface-active compounds to the organic surface layer where it can induce radical reactions, leading to the formation of a variety of compounds. We also identified photoproducts at the water-air interface that cannot be assigned by the bulk analysis. Under the environmental conditions applied in this work, the 4-BBA was found to be acting as a source of photoproducts in addition to its expected role as a photosensitizer for the NA. The photolysis of the 4-BBA is more active when exposed to shorter wavelengths of the UV portion of the light spectrum. The subsequent reactions between the photoproducts can lead to the formation of aromatic compounds, including compounds with amphipathic structures that are surface-active and responsible for the restructuring of the water molecules at the interface. Lower pH values were found to be more favorable for the formation of these amphipathic aromatic compounds.

The spectral power distribution of the irradiation light significantly affects the photoreactions. The shorter wavelength and/or higher intensity has a stronger effect. The change in pH changes the concentration of partially dissociated fatty acids at the surface and influences the photoreaction rate and possibly pathways. Preliminary results also showed that the salinity accelerates the photoreaction rate. We attribute this effect to the increase in the concentration of the 4-BBA at the air-water interface caused by the bulk dissolved salts. Further investigation of the mechanism under varying pH and salty conditions is necessary to be addressed in future work. Finally, dissolved oxygen develops multiple pathways of the interactions. While our study provides valuable mechanistic insight, broader conclusions would require further investigation using additional model systems and environmentally relevant mixtures. In nature, these processes are even more complex due to the presence of a large variety of fatty acids at the SML which enrich more organic photosensitizers at the surface. Similar photochemistry can apply to all water surfaces, e.g., ocean, rivers, lakes, and even cloud droplets.

Data availability. The data used in this study are available from the corresponding author upon request (ahmed.abdelmonem@kit.edu).

Supplement. Supplementary information related to this manuscript, including additional figures, tables, and experimental procedures, is provided to support and enhance the understanding of the study. These materials offer further insight into the methods and results discussed in the main text, ensuring a comprehensive overview of the research. The supplement related to this article is available online at https://doi.org/10.5194/acp-25-13019-2025-supplement.

Author contributions. All authors have made significant contributions to this research. AA proposed the research idea, conducted the literature review, designed and built the custom solar simulator, and conceived and designed the experiments. AA led the SFG and MS experiments, performed data analysis and interpretation, and wrote and compiled the manuscript. DG conducted the SFG experiments alongside AA, contributed to the SFG data analysis, and provided critical revisions to the manuscript. DG additionally revised and corrected the chemical composition part of the MS study after the referees' reports. YG performed the MS experiments, analyzed and interpreted the MS data in collaboration with AA, and drafted the MS-related sections. BB supervised the SFG experiments, discussed the results with AA and DG, and reviewed the SFG-related sections. HS supervised the MS experiments, discussed the results with AA and YG, and revised the MS sections. JL contributed to the chemistry aspects of the experiments, assisted with methodology development and data collection, and participated in manuscript revisions. MF supported the estimation and validation of the solar simulator output and characteristics and assisted in final manuscript preparation.

Competing interests. At least one of the (co-)authors is a member of the editorial board of *Atmospheric Chemistry and Physics*. The peer-review process was guided by an independent editor, and the authors also have no other competing interests to declare.

Disclaimer. Publisher's note: Copernicus Publications remains neutral with regard to jurisdictional claims made in the text, published maps, institutional affiliations, or any other geographical representation in this paper. While Copernicus Publications makes every effort to include appropriate place names, the final responsibility lies with the authors. Views expressed in the text are those of the authors and do not necessarily reflect the views of the publisher.

Acknowledgements. Ahmed Abdelmonem gratefully acknowledges the support of the German Research Foundation (DFG, AB 604/3-1). Special thanks are extended to Ottmar Möhler for hosting Ahmed Abdelmonem in his group at KIT during the finalization of the manuscript following the conclusion of the DFG project. The authors thank Olga Dombrowski for assistance with sample preparations in the chemistry lab at KIT and Thomas Leis-

ner for hosting the first author at IMKAAF-KIT during the DFG project period. Dana Glikman and Björn Braunschweig thank the DFG for funding CRC 1459 Intelligent Matter – Project-ID 433682494. The authors acknowledge the assistance of Chat-GPT in refining the abstract, author contributions, and acknowledgments text for improved clarity and professionalism in an earlier draft.

Financial support. This research has been supported by the Deutsche Forschungsgemeinschaft (grant no. AB 604/3-1).

The article processing charges for this open-access publication were covered by the Karlsruhe Institute of Technology (KIT).

Review statement. This paper was edited by Theodora Nah and reviewed by Liselotte Tinel and two anonymous referees.

References

- Alpert, P. A., Ciuraru, R., Rossignol, S., Passananti, M., Tinel, L., Perrier, S., Dupart, Y., Steimer, S. S., Ammann, M., Donaldson, D. J., and George, C.: Fatty Acid Surfactant Photochemistry Results in New Particle Formation, Sci. Rep.-UK, 7, https://doi.org/10.1038/s41598-017-12601-2, 2017.
- Atkinson, R.: Atmospheric chemistry of VOCs and NO_x , Atmos. Environ., 34, 2063–2101, https://doi.org/10.1016/S1352-2310(99)00460-4, 2000.
- Backus, E. H. G., Bonn, D., Cantin, S., Roke, S., and Bonn, M.: Laser-Heating-Induced Displacement of Surfactants on the Water Surface, J. Phys. Chem. B, 116, 2703–2712, https://doi.org/10.1021/jp2074545, 2012.
- Badban, S., Hyde, A. E., and Phan, C. M.: Hydrophilicity of Nonanoic Acid and Its Conjugate Base at the Air/Water Interface, ACS Omega, 2, 5565–5573, https://doi.org/10.1021/acsomega.7b00960, 2017.
- Bernard, F., Ciuraru, R., Boréave, A., and George, C.: Photosensitized Formation of Secondary Organic Aerosols above the Air/Water Interface, Environ. Sci. Technol., 50, 8678–8686, https://doi.org/10.1021/acs.est.6b03520, 2016.
- Boucher, O.: Atmospheric Aerosols, in: Atmospheric Aerosols: Properties and Climate Impacts, edited by: Boucher, O., Springer Netherlands, Dordrecht, https://doi.org/10.1007/978-94-017-9649-1_2, 9-24, 2015.
- Brüggemann, M., Hayeck, N., and George, C.: Interfacial photochemistry at the ocean surface is a global source of organic vapors and aerosols, Nat. Commun., 9, 2101, https://doi.org/10.1038/s41467-018-04528-7, 2018.
- Carlson, D. J.: Dissolved organic materials in surface microlayers: Temporal and spatial variability and relation to sea state, Limnol. Oceanogr., 28, 415–431, https://doi.org/10.4319/lo.1983.28.3.0415, 1983.
- Carlson, D. J. and Mayer, L. M.: Enrichment of dissolved phenolic material in the surface microlayer of coastal waters, Nature, 286, 482–483, https://doi.org/10.1038/286482a0, 1980.

- Carpenter, L. J. and Nightingale, P. D.: Chemistry and Release of Gases from the Surface Ocean, Chem. Rev., 115, 4015–4034, https://doi.org/10.1021/cr5007123, 2015.
- Ciuraru, R., Fine, L., van Pinxteren, M., D'Anna, B., Herrmann, H., and George, C.: Photosensitized production of functionalized and unsaturated organic compounds at the air-sea interface, Sci. Rep.-UK, 5, 12741, https://doi.org/10.1038/srep12741, 2015.
- Covington, A. K. and Whitfield, M.: Recommendations for the determination of pH in sea water and estuarine waters, Pure Appl. Chem., 60, 865–870, https://doi.org/10.1351/pac198860060865, 1988.
- Cui, G., Liu, Y., and Tong, S.: Hydrogeochemical processes controlling the salinity of surface water and groundwater in an inland saline-alkali wetland in western Jilin, China, Front. Ecol. Evol., 10, https://doi.org/10.3389/fevo.2022.993849, 2022.
- Dalton, E. Z., Wang, X., Wappes, S. C., Petersen-Sonn, E. A., Hagan, S. N., George, C., and Raff, J. D.: Photosensitizers Regulate Nitrate Photoproduct Yields in Bulk Aqueous Matrices, Environ. Sci. Technol., 59, 6142–6154, https://doi.org/10.1021/acs.est.4c09491, 2025.
- Dickson, A. G.: The measurement of sea water pH, Mar. Chem., 44, 131–142, https://doi.org/10.1016/0304-4203(93)90198-W, 1993.
- Dommer, A. C., Rogers, M. M., Carter-Fenk, K. A., Wauer, N. A., Rubio, P., Davasam, A., Allen, H. C., and Amaro, R. E.: Interfacial Enrichment of Lauric Acid Assisted by Long-Chain Fatty Acids, Acidity and Salinity at Sea Spray Aerosol Surfaces, J. Phys. Chem. A, 128, 7195–7207, https://doi.org/10.1021/acs.jpca.4c03335, 2024.
- Doughty, B., Yin, P. C., and Ma, Y. Z.: Adsorption, Ordering, and Local Environments of Surfactant-Encapsulated Polyoxometalate Ions Probed at the Air-Water Interface, Langmuir, 32, 8116–8122, https://doi.org/10.1021/acs.langmuir.6b01643, 2016.
- Freeman-Gallant, G., Davis, E. J., Scholer, E., Alija, O., and Navea, J. G.: Photooxidation of Nonanoic Acid by Molecular and Complex Environmental Photosensitizers, J. Phys. Chem. A, 128, 9792–9803, https://doi.org/10.1021/acs.jpca.4c05608, 2024.
- Gantt, B. and Meskhidze, N.: The physical and chemical characteristics of marine primary organic aerosol: a review, Atmos. Chem. Phys., 13, 3979–3996, https://doi.org/10.5194/acp-13-3979-2013, 2013.
- García Rey, N., Weißenborn, E., Schulze-Zachau, F., Gochev, G., and Braunschweig, B.: Quantifying Double-Layer Potentials at Liquid–Gas Interfaces from Vibrational Sum-Frequency Generation, J. Phys. Chem. C, 123, 1279–1286, https://doi.org/10.1021/acs.jpcc.8b10097, 2019.
- Gautam, K. S., Schwab, A. D., Dhinojwala, A., Zhang, D., Dougal, S. M., and Yeganeh, M. S.: Molecular Structure of Polystyrene at Air/Polymer and Solid/Polymer Interfaces, Phys. Rev. Lett., 85, 3854–3857, https://doi.org/10.1103/PhysRevLett.85.3854, 2000.
- Ghosh, A., Campen, R. K., Sovago, M., and Bonn, M.: Structure and dynamics of interfacial water in model lung surfactants, Faraday Discuss., 141, 145–159, https://doi.org/10.1039/b805858j, 2009.
- Goswami, P. C., Mayo, P. de, Ramnath, N., Bernard, G., Omkaram, N., Scheffer, J. R., and Wong, Y.-F.: Modification of photochemical reactivity through the use of clathrates: the Norrish type I and type II reactions in Dianin's compound, Can. J. Chem., 63, 2719–2725, https://doi.org/10.1139/v85-451, 1985.

- Gragson, D. E. and Richmond, G. L.: Investigations of the Structure and Hydrogen Bonding of Water Molecules at Liquid Surfaces by Vibrational Sum Frequency Spectroscopy, J. Phys. Chem. B, 102, 3847–3861, https://doi.org/10.1021/jp9806011, 1998.
- Hardt, M., Honnigfort, C., Carrascosa-Tejedor, J., Braun, M. G., Winnall, S., Glikman, D., Gutfreund, P., Campbell, R. A., and Braunschweig, B.: Photoresponsive arylazopyrazole surfactant/PDADMAC mixtures: reversible control of bulk and interfacial properties, Nanoscale, 16, 9975–9984, https://doi.org/10.1039/D3NR05414D, 2024.
- Hendrickson, B. N., Brooks, S. D., Thornton, D. C. O., Moore, R. H., Crosbie, E., Ziemba, L. D., Carlson, C. A., Baetge, N., Mirrielees, J. A., and Alsante, A. N.: Role of Sea Surface Microlayer Properties in Cloud Formation, Front. Mar. Sci., 7, https://doi.org/10.3389/fmars.2020.596225, 2021.
- Henry, M. C., Yang, Y. J., Pizzolatto, R. L., and Messmer, M. C.: Competitive adsorption of 2,4,7,9-tetramethyl-5-decyn-4,7-diol and linear alkane surfactants at the air/water interface, Langmuir, 19, 2592–2598, https://doi.org/10.1021/la0268121, 2003.
- Jiang, L. Q., Carter, B. R., Feely, R. A., Lauvset, S. K., and Olsen, A.: Surface ocean pH and buffer capacity: past, present and future, Sci. Rep.-UK, 9, 18624, https://doi.org/10.1038/s41598-019-55039-4, 2019.
- Jiménez, M. C. and Miranda, M. A.: Organic aspects. Oxygencontaining functions, Royal Society of Chemistry, 169–193, https://doi.org/10.1039/9781788013598-00169, 2018.
- Kroll, J. H., Lim, C. Y., Kessler, S. H., and Wilson, K. R.: Heterogeneous Oxidation of Atmospheric Organic Aerosol: Kinetics of Changes to the Amount and Oxidation State of Particle-Phase Organic Carbon, J. Phys. Chem. A, 119, 10767–10783, https://doi.org/10.1021/acs.jpca.5b06946, 2015.
- Kusaka, R., Ishiyama, T., Nihonyanagi, S., Morita, A., and Tahara, T.: Structure at the air/water interface in the presence of phenol: a study using heterodyne-detected vibrational sum frequency generation and molecular dynamics simulation, Phys. Chem. Chem. Phys., 20, 3002–3009, https://doi.org/10.1039/C7CP05150F, 2018.
- Lankone, R. S., Deline, A. R., Barclay, M., and Fairbrother, D. H.: UV–Vis quantification of hydroxyl radical concentration and dose using principal component analysis, Talanta, 218, 121148, https://doi.org/10.1016/j.talanta.2020.121148, 2020.
- Liss, P. S. and Duce, R. A.: The Sea Surface and Global Change, Cambridge University Press, ISBN 9780521017459, ISBN 0521017459, 2005.
- Lu, R., Gan, W., Wu, B., Zhang, Z., Guo, Y., and Wang, H.: C-H Stretching Vibrations of Methyl, Methylene and Methine Groups at the Vapor/Alcohol (n=1-8) Interfaces, J. Phys. Chem. B, 109, 14118–14129, https://doi.org/10.1021/jp051565q, 2005.
- MacPhail, R. A., Strauss, H. L., Snyder, R. G., and Elliger, C. A.: Carbon-hydrogen stretching modes and the structure of n-alkyl chains. 2. Long, all-trans chains, J. Phys. Chem., 88, 334–341, https://doi.org/10.1021/j150647a002, 1984.
- Marion, G. M., Millero, F. J., Camões, M. F., Spitzer, P., Feistel, R., and Chen, C. T. A.: pH of seawater, Mar. Chem., 126, 89–96, https://doi.org/10.1016/j.marchem.2011.04.002, 2011.
- Meerkötter, R. and Vázquez-Navarro, M.: Earth's Radiation Budget: The Driver for Weather and Climate, in: Atmospheric Physics: Background Methods Trends, edited by: Schu-

- mann, U., Springer Berlin Heidelberg, Berlin, Heidelberg, https://doi.org/10.1007/978-3-642-30183-4_4, 55-67, 2012.
- Milinković, A., Penezić, A., Kušan, A. C., Gluščić, V., Žužul, S., Skejić, S., Šantić, D., Godec, R., Pehnec, G., Omanović, D., Engel, A., and Frka, S.: Variabilities of biochemical properties of the sea surface microlayer: Insights to the atmospheric deposition impacts, Sci. Total Environ., 838, 156440, https://doi.org/10.1016/j.scitotenv.2022.156440, 2022.
- Millero, F. J., Feistel, R., Wright, D. G., and McDougall, T. J.: The composition of Standard Seawater and the definition of the Reference-Composition Salinity Scale, Deep-Sea Res. Part I Oceanogr. Res. Pap., 55, 50–72, https://doi.org/10.1016/j.dsr.2007.10.001, 2008.
- Miranda, P. B. and Shen, Y. R.: Liquid interfaces: A study by sum-frequency vibrational spectroscopy, J. Phys. Chem. B, 103, 3292–3307, https://doi.org/10.1021/jp9843757, 1999.
- Mmereki, B. T. and Donaldson, D. J.: Laser induced fluorescence of pyrene at an organic coated air–water interface, Phys. Chem. Chem. Phys., 4, 4186–4191, https://doi.org/10.1039/b204754c, 2002.
- Mora Garcia, S. L., Pandit, S., Navea, J. G., and Grassian, V. H.: Nitrous Acid (HONO) Formation from the Irradiation of Aqueous Nitrate Solutions in the Presence of Marine Chromophoric Dissolved Organic Matter: Comparison to Other Organic Photosensitizers, ACS Earth Sp. Chem., 5, 3056–3064, https://doi.org/10.1021/acsearthspacechem.1c00292, 2021.
- Morgan, J. J.: Aquatic Chemistry-Chemical Equilibria and Rates in Natural Waters, John Wiley, USA, ISBN 9780471511854, ISBN 0471511854, 1995.
- Nihonyanagi, S., Mondal, J. A., Yamaguchi, S., and Tahara, T.: Structure and dynamics of interfacial water studied by heterodyne-detected vibrational sum-frequency generation, Annu. Rev. Phys. Chem., 64, 579–603, https://doi.org/10.1146/annurev-physchem-040412-110138, 2013.
- Numadate, N., Saito, S., Nojima, Y., Ishibashi, T., Enami, S., and Hama, T.: Direct Observation and Quantitative Measurement of OH Radical Desorption During the Ultraviolet Photolysis of Liquid Nonanoic Acid, J. Phys. Chem. Lett., 13, 8290–8297, https://doi.org/10.1021/acs.jpclett.2c02199, 2022.
- Ouafo-Leumbe, M. R., Galy-Lacaux, C., Liousse, C., Pont, V., Akpo, A., Doumbia, T., Gardrat, E., Zouiten, C., Sigha-Nkamdjou, L., and Ekodeck, G. E.: Chemical composition and sources of atmospheric aerosols at Djougou (Benin), Meteorol. Atmos. Phys., 130, 591–609, https://doi.org/10.1007/s00703-017-0538-5, 2018.
- Rao, Y., Li, X., Lei, X. G., Jockusch, S., George, M. W., Turro, N. J., and Eisenthal, K. B.: Observations of Interfacial Population and Organization of Surfactants with Sum Frequency Generation and Surface Tension, J. Phys. Chem. C, 115, 12064–12067, https://doi.org/10.1021/jp201799z, 2011.
- Riva, M., Rantala, P., Krechmer, J. E., Peräkylä, O., Zhang, Y., Heikkinen, L., Garmash, O., Yan, C., Kulmala, M., Worsnop, D., and Ehn, M.: Evaluating the performance of five different chemical ionization techniques for detecting gaseous oxygenated organic species, Atmos. Meas. Tech., 12, 2403–2421, https://doi.org/10.5194/amt-12-2403-2019, 2019.
- Schultz, M. J., Baldelli, S., Schnitzer, C., and Simonelli, D.: Aqueous Solution/Air Interfaces Probed with Sum Frequency

- Generation Spectroscopy, J. Phys. Chem. B, 106, 5313–5324, https://doi.org/10.1021/jp014466v, 2002.
- Sellegri, K., O'Dowd, C. D., Yoon, Y. J., Jennings, S. G., and de Leeuw, G.: Surfactants and submicron sea spray generation, J. Geophys. Res., 111, https://doi.org/10.1029/2005jd006658, 2006.
- Sellegri, K., Simó, R., Wang, B., Alpert, P. A., Altieri, K., Burrows, S., Hopkins, F. E., Koren, I., McCoy, I. L., Ovadnevaite, J., Salter, M., and Schmale, J.: Influence of open ocean biogeochemistry on aerosol and clouds: Recent findings and perspectives, Elementa Sci. Anth., 12, https://doi.org/10.1525/elementa.2023.00058, 2024.
- Shen, Y. R.: Surface Properties Probed by Second-Harmonic and Sum-Frequency Generation, Nature, 337, 519–525, https://doi.org/10.1038/337519a0, 1989.
- Shultz, M. J., Schnitzer, C., Simonelli, D., and Baldelli, S.: Sum frequency generation spectroscopy of the aqueous interface: ionic and soluble molecular solutions, Int. Rev. Phys. Chem., 19, 123–153, https://doi.org/10.1080/014423500229882, 2000.
- Snyder, R. G., Strauss, H. L., and Elliger, C. A.: Carbon-hydrogen stretching modes and the structure of n-alkyl chains. 1. Long, disordered chains, J. Phys. Chem., 86, 5145–5150, https://doi.org/10.1021/j100223a018, 1982.
- Sovago, M., Campen, R. K., Wurpel, G. W. H., Müller, M., Bakker, H. J., and Bonn, M.: Vibrational Response of Hydrogen-Bonded Interfacial Water is Dominated by Intramolecular Coupling, Phys. Rev. Lett., 100, 173901, https://doi.org/10.1103/PhysRevLett.100.173901, 2008.
- Stolle, C., Ribas-Ribas, M., Badewien, T. H., Barnes, J., Carpenter, L. J., Chance, R., Damgaard, L. R., Durán Quesada, A. M., Engel, A., Frka, S., Galgani, L., Gašparović, B., Gerriets, M., Hamizah Mustaffa, N. I., Herrmann, H., Kallajoki, L., Pereira, R., Radach, F., Revsbech, N. P., Rickard, P., Saint, A., Salter, M., Striebel, M., Triesch, N., Uher, G., Upstill-Goddard, R. C., van Pinxteren, M., Zäncker, B., Zieger, P., and Wurl, O.: The MILAN Campaign: Studying Diel Light Effects on the Air–Sea Interface, B. Am. Meteorol. Soc., 101, E146–E166, https://doi.org/10.1175/BAMS-D-17-0329.1, 2020.
- Tilstone, G. H., Airs, ruth L., Vicente, V. M., Widdicombe, C., and Llewellyn, C.: High concentrations of mycosporine-like amino acids and colored dissolved organic matter in the sea surface microlayer off the Iberian Peninsula, Limnol. Oceanogr., 55, 1835–1850, https://doi.org/10.4319/lo.2010.55.5.1835, 2010.
- Tinel, L., Rossignol, S., Bianco, A., Passananti, M., Perrier, S., Wang, X., Brigante, M., Donaldson, D. J., and George, C.: Mechanistic Insights on the Photosensitized Chemistry of a Fatty Acid at the Air/Water Interface, Environ. Sci. Technol., 50, 11041–11048, https://doi.org/10.1021/acs.est.6b03165, 2016.
- Tinel, L., Abbatt, J., Saltzman, E., Engel, A., Fernandez, R., Li, Q., Mahajan, A. S., Nicewonger, M., Novak, G., Saiz-Lopez, A., Schneider, S., and Wang, S.: Impacts of ocean biogeochemistry on atmospheric chemistry, Elementa Sci. Anth., 11, https://doi.org/10.1525/elementa.2023.00032, 2023.
- Truong, V. N. T., Wang, X. M., Dang, L. X., and Miller, J. D.: Interfacial Water Features at Air-Water Interfaces as Influenced by Charged Surfactants, J. Phys. Chem. B, 123, 2397–2404, https://doi.org/10.1021/acs.jpcb.9b01246, 2019.
- van Pinxteren, M., Fomba, K. W., Triesch, N., Stolle, C., Wurl, O., Bahlmann, E., Gong, X., Voigtländer, J., Wex, H., Robinson,

- T.-B., Barthel, S., Zeppenfeld, S., Hoffmann, E. H., Roveretto, M., Li, C., Grosselin, B., Daële, V., Senf, F., van Pinxteren, D., Manzi, M., Zabalegui, N., Frka, S., Gašparović, B., Pereira, R., Li, T., Wen, L., Li, J., Zhu, C., Chen, H., Chen, J., Fiedler, B., von Tümpling, W., Read, K. A., Punjabi, S., Lewis, A. C., Hopkins, J. R., Carpenter, L. J., Peeken, I., Rixen, T., Schulz-Bull, D., Monge, M. E., Mellouki, A., George, C., Stratmann, F., and Herrmann, H.: Marine organic matter in the remote environment of the Cape Verde islands an introduction and overview to the MarParCloud campaign, Atmos. Chem. Phys., 20, 6921–6951, https://doi.org/10.5194/acp-20-6921-2020, 2020.
- Varga, I., Keszthelyi, T., Meszaros, R., Hakkel, O., and Gilanyi, T.: Observation of a liquid-gas phase transition in monolayers of alkyltrimethylammonium alkyl sulfates adsorbed at the air/water interface, J. Phys. Chem. B, 109, 872–878, https://doi.org/10.1021/jp0480060, 2005.
- Wang, Y., Zeng, J., Wu, B., Song, W., Hu, W., Liu, J., Yang, Y., Yu, Z., Wang, X., and Gligorovski, S.: Production of Volatile Organic Compounds by Ozone Oxidation Chemistry at the South China Sea Surface Microlayer, ACS Earth Sp. Chem., 7, 1306–1313, https://doi.org/10.1021/acsearthspacechem.3c00102, 2023.
- Wilson, T. W., Ladino, L. A., Alpert, P. A., Breckels, M. N., Brooks,
 I. M., Browse, J., Burrows, S. M., Carslaw, K. S., Huffman,
 J. A., Judd, C., Kilthau, W. P., Mason, R. H., McFiggans, G.,
 Miller, L. A., Najera, J. J., Polishchuk, E., Rae, S., Schiller,
 C. L., Si, M., Temprado, J. V, Whale, T. F., Wong, J. P. S.,
 Wurl, O., Yakobi-Hancock, J. D., Abbatt, J. P. D., Aller, J. Y.,
 Bertram, A. K., Knopf, D. A., and Murray, B. J.: A marine
 biogenic source of atmospheric ice-nucleating particles, Nature,
 525, https://doi.org/10.1038/nature14986, 2015.
- Xing, J., Zheng, S., Li, S., Huang, L., Wang, X., Kelly, J. T., Wang, S., Liu, C., Jang, C., Zhu, Y., Zhang, J., Bian, J., Liu, T.-Y., and Hao, J.: Mimicking atmospheric photochemical modeling with a deep neural network, Atmos. Res., 265, 105919, https://doi.org/10.1016/j.atmosres.2021.105919, 2022.
- Yan, S., Liu, Y., Lian, L., Li, R., Ma, J., Zhou, H., and Song, W.: Photochemical formation of carbonate radical and its reaction with dissolved organic matters, Water Res., 161, 288–296, https://doi.org/10.1016/j.watres.2019.06.002, 2019.
- Yang, L., Zhang, J., Engel, A., and Yang, G.-P.: Spatio-temporal distribution, photoreactivity and environmental control of dissolved organic matter in the sea-surface microlayer of the eastern marginal seas of China, Biogeosciences, 19, 5251–5268, https://doi.org/10.5194/bg-19-5251-2022, 2022.
- You, B., Li, S., Tsona, N. T., Li, J., Xu, L., Yang, Z., Cheng, S., Chen, Q., George, C., Ge, M., and Du, L.: Environmental Processing of Short-Chain Fatty Alcohols Induced by Photosensitized Chemistry of Brown Carbons, ACS Earth Sp. Chem., 4, 631–640, https://doi.org/10.1021/acsearthspacechem.0c00023, 2020.
- Zhang, D., Gutow, J., and Eisenthal, K. B.: Vibrational-spectra, orientations, and phase-transitions in long-chain amphiphiles at the air-water-interface probing the head and tail groups by sum-frequency generation, J. Phys. Chem., 98, 13729–13734, https://doi.org/10.1021/j100102a045, 1994.